


Giant proximity exchange and valley splitting in transition metal dichalcogenide/*h*BN/(Co, Ni) heterostructures

Klaus Zollner ^{*}, Paulo E. Faria Junior, and Jaroslav Fabian

Institute for Theoretical Physics, University of Regensburg, 93040 Regensburg, Germany



(Received 29 October 2019; revised manuscript received 21 January 2020; accepted 23 January 2020; published 10 February 2020)

We investigate the proximity-induced exchange coupling in transition-metal dichalcogenides (TMDCs), originating from spin injector geometries composed of hexagonal boron-nitride (*h*BN) and ferromagnetic (FM) cobalt (Co) or nickel (Ni), from first principles. We employ a minimal tight-binding Hamiltonian that captures the low energy bands of the TMDCs around *K* and *K'* valleys, to extract orbital, spin-orbit, and exchange parameters. The TMDC/*h*BN/FM heterostructure calculations show that due to the *h*BN buffer layer, the band structure of the TMDC is preserved, with an additional proximity-induced exchange splitting in the bands. We extract proximity exchange parameters in the 1–10 meV range, depending on the FM. The combination of proximity-induced exchange and intrinsic spin-orbit coupling (SOC) of the TMDCs, leads to a valley polarization, translating into magnetic exchange fields of tens of Tesla. The extracted parameters are useful for subsequent exciton calculations of TMDCs in the presence of a *h*BN/FM spin injector. Our calculated absorption spectra show large splittings for the exciton peaks; in the case of MoS₂/*h*BN/Co we find a value of about 8 meV, corresponding to about 50 T external magnetic field in bare TMDCs. The reason lies in the band structure, where a hybridization with Co *d* orbitals causes a giant valence band exchange splitting of more than 10 meV. Structures with Ni do not show any *d* level hybridization features, but still sizable proximity exchange and exciton peak splittings of around 2 meV are present in the TMDCs.

DOI: [10.1103/PhysRevB.101.085112](https://doi.org/10.1103/PhysRevB.101.085112)

I. INTRODUCTION

Spintronics is based on the efficient injection, transport, manipulation, and detection of spins in a material [1–3]. The current generation of spintronics devices employ hybrid geometries consisting of several two-dimensional (2D) materials [4,5] in order to overcome intrinsic limitations of the transport medium. A new branch of physics has emerged, which is solely dedicated to the interface engineering [6,7] of those ultrathin layers, including semiconductors, ferromagnets, and superconductors, leading to new device technologies.

The most prominent example in this field is graphene, which has intrinsically outstanding spin and charge transport properties. For several years now, physicists have studied graphene based spintronics devices [2] and have found an efficient way to inject spins via FM/insulator tunnel junctions into graphene [8–13]. Nonlocal measurement geometries reveal the spin transport properties of graphene, which can be modified by the presence of various 2D materials in van der Waals heterostructures. Currently, state of the art spin transport geometries are based on *h*BN encapsulated graphene [10,12,14,15], where spins are injected by FMs, with giant mobilities up to 10⁶ cm²/V s [16–18] and spin lifetimes exceeding 10 ns [10]. The insulating *h*BN is ideal to reduce the contact resistance to the FM and helps to preserve the linear dispersion of graphene, which is desired for spin transport [19]. Also oxide insulators are used, such as MgO and SiO₂, resulting in less efficient spin injection [14]. The manipulation

of spins can be achieved by inducing SOC or exchange coupling from proximity. For example, a TMDC in proximity to graphene induces strong valley Zeeman spin-orbit fields on the order of 1 meV [20–22], significantly reducing spin lifetimes in graphene to about 10 ps [23–25], but leading to giant spin relaxation anisotropies (the ratio of out-of-plane to in-plane spin lifetime) of about 10 [22–27]. Additionally, it has been demonstrated that a TMDC can be utilized for optical spin injection in graphene [21,25,28], relevant for the field of optospintronics.

Recently, there has been a lot of effort to use also other 2D materials such as phosphorene or TMDCs as the transport medium. The advantage is that they are already semiconducting, making them suitable for electronic and spintronic devices [1,3], such as spin diodes and field effect transistors [29–32]. In the case of phosphorene, very little is known about its spin transport properties [33–35]; the electronic ones are highly anisotropic and show large mobilities [36,37]. Furthermore, measurements combined with first-principles calculations show that *h*BN is also an ideal tunnel barrier, when injecting spin polarized carriers from Co into phosphorene [35].

Monolayer TMDCs have a band gap in the optical range and the valley degree of freedom plays a major role [38–43] in their (opto-) electronic properties. The helicity selective excitation of carriers with certain spin in a certain valley at the same excitation energy, makes those materials very attractive for the field of valleytronics [44–48]. By an exchange field one can break the time-reversal symmetry of the TMDC, the degeneracy of the valleys, and introduce valley polarization.

*klaus.zollner@physik.uni-regensburg.de

In an external magnetic field, the valley splitting rises roughly linear with 0.1–0.2 meV/T [49–52], such that large fields are required to get a sizable effect. A much better perspective to achieve large valley polarization in TMDCs is by the proximity exchange effect. Indeed, placing the TMDC on a magnetic substrate, giant valley splittings can be achieved, ranging from a few to hundreds of meV [47,48,53–61], which can additionally be tuned by gating and twisting [62].

For spin injection, one can either contact the TMDC with metal or metal/insulator interfaces or inject them optically [63,64]. In the former case, studying the dependence of the Schottky barrier on the used electrode is crucial [65–72]. It turns out that a h BN tunnel barrier is also a good choice here, preserving the intrinsic properties of the TMDC while enormously reducing the contact resistance [66,73–75]. Also other insulating barriers, such as TiO_2 , MgO , or Al_2O_3 [76–80], are promising candidates, where the thickness of the barrier plays an important role for the efficiency of spin injection. The contact resistance can also be decreased by strong electron doping [81] or using graphene electrodes [82].

Electronic and spin transport [83–86] in TMDCs is becoming an important topic. It has been shown that the carrier mobility increases with the number of TMDC layers [70,85], due to reduced Coulomb scattering in thicker samples [87], while phonon scattering limits the room temperature mobility [86]. Spin transport has been studied on a theoretical level [88–91], while spin injection has been demonstrated electrically [47,77] and optically [64], showing spin diffusion lengths of about 200 nm in multilayer TMDCs [77].

A very natural choice for spin injection and for generating proximity exchange in TMDCs are h BN/FM tunnel structures. How large is the proximity-induced exchange in TMDC/ h BN/FM heterostructures? What are the optical signatures of such structures? In this paper we study TMDC/ h BN/FM tunneling spin injection heterostructures. We calculate the band structure and employ a minimal tight-binding model Hamiltonian to extract orbital, spin-orbit, and proximity exchange parameters for the proximitized TMDCs, MoS_2 , and WS_2 . Proximity exchange in the TMDCs is found to be on the order of 1–10 meV, and together with the intrinsic SOC of the TMDC, leads to a valley polarization corresponding to tens of Tesla exchange field for bare TMDCs. Specifically the $\text{MoS}_2/h\text{BN}/\text{Co}$ heterostructure shows a giant valence band spin splitting, of more than 10 meV, due to proximity exchange and hybridization of the TMDC valence band orbitals with Co d orbitals. The corresponding calculated absorption spectrum shows a giant valley splitting of about 8 meV. The valley splitting for $\text{WS}_2/h\text{BN}/\text{Co}$ is of similar magnitude (5 meV), despite the absence of hybridizing d orbitals. In the case of Ni, proximity exchange and valley splittings are reduced (1–3 meV) for both TMDCs. Our investigations should be useful for interpreting spin injection, spin tunneling, and optical properties of TMDC/ h BN/(Co, Ni) systems. Furthermore, the extracted parameters can be used for transport simulations and further studies of excitonic effects.

II. MODEL HAMILTONIAN

As basis states for our model we use $|\Psi_{\text{CB}}\rangle = |d_{z^2}\rangle$ and $|\Psi_{\text{VB}}^\tau\rangle = \frac{1}{\sqrt{2}}(|d_{x^2-y^2}\rangle + i\tau|d_{xy}\rangle)$, corresponding to con-

duction band (CB) and valence band (VB) at K ($\tau = 1$) and K' ($\tau = -1$), since the band edges of bare TMDC monolayers are formed by different d orbitals from the transition metal [38]. The model Hamiltonian, in the basis which includes electron spin $|\Psi_{\text{CB}}, \uparrow\rangle$, $|\Psi_{\text{VB}}, \uparrow\rangle$, $|\Psi_{\text{CB}}, \downarrow\rangle$, and $|\Psi_{\text{VB}}, \downarrow\rangle$, to describe the band structure of the TMDC close to K and K' , in the presence of proximity exchange [55,62] is

$$\mathcal{H} = \mathcal{H}_0 + \mathcal{H}_\Delta + \mathcal{H}_{\text{soc}} + \mathcal{H}_{\text{ex}} + \mathcal{H}_{\text{R}}, \quad (1)$$

$$\mathcal{H}_0 = \hbar v_{\text{F}} s_0 \otimes (\tau \sigma_x k_x + \sigma_y k_y), \quad (2)$$

$$\mathcal{H}_\Delta = \frac{\Delta}{2} s_0 \otimes \sigma_z, \quad (3)$$

$$\mathcal{H}_{\text{soc}} = \tau s_z \otimes (\lambda_c \sigma_+ + \lambda_v \sigma_-), \quad (4)$$

$$\mathcal{H}_{\text{ex}} = -s_z \otimes (B_c \sigma_+ + B_v \sigma_-), \quad (5)$$

$$\mathcal{H}_{\text{R}} = \lambda_{\text{R}} (\tau s_y \otimes \sigma_x - s_x \otimes \sigma_y). \quad (6)$$

Here v_{F} is the Fermi velocity. The Cartesian components k_x and k_y of the electron wave vector are measured from K (K'). The pseudospin Pauli matrices are σ_i acting on the (CB,VB) subspace and spin Pauli matrices are s_i acting on the (\uparrow, \downarrow) subspace, with $i = \{0, x, y, z\}$. For shorter notation we introduce $\sigma_\pm = \frac{1}{2}(\sigma_0 \pm \sigma_z)$. TMDCs are semiconductors, and thus \mathcal{H}_Δ introduces a gap, represented by parameter Δ , in the band structure such that $\mathcal{H}_0 + \mathcal{H}_\Delta$ describes a gapped spectrum with spin-degenerate parabolic CB and VB. In addition, the bands are spin split due to SOC which is captured by the term \mathcal{H}_{soc} with the parameters λ_c and λ_v describing the spin splitting of the CB and VB. The Hamiltonian $\mathcal{H}_0 + \mathcal{H}_\Delta + \mathcal{H}_{\text{soc}}$ is already suitable to describe the spectrum of intrinsic TMDCs around the band edges at K and K' . In the case when we have a ferromagnetic substrate, proximity exchange effects are present and we introduce the term \mathcal{H}_{ex} , with B_c and B_v describing the proximity induced exchange splittings. Note that this term explicitly breaks time-reversal symmetry and thus the valley degeneracy. Finally, a Rashba term \mathcal{H}_{R} , with λ_{R} being the Rashba parameter, can be present since a substrate breaks the inversion symmetry of the TMDC.

III. COMPUTATIONAL DETAILS

A. First-principles calculations

The electronic structure calculations and structural relaxation of our geometries are performed with density functional theory (DFT) [92] using QUANTUM ESPRESSO [93]. Self-consistent calculations are performed with the k -point sampling of $18 \times 18 \times 1$ for the TMDC/ h BN/FM heterostructures. We perform open shell calculations that provide the spin polarized ground state, when a FM substrate is present. We use an energy cutoff for charge density of 550 Ry, and the kinetic energy cutoff for wave functions is 65 Ry for the scalar relativistic pseudopotential with the projector augmented wave method [94] with the Perdew-Burke-Ernzerhof exchange correlation functional [95]. When SOC is included, the fully relativistic versions of the pseudopotentials are used. In addition we include the Hubbard correction for the FMs Co and Ni with $U = 1$ eV [96]. For this value of the Hubbard

U , the calculated magnetic moments of Co and Ni in our slab geometry are comparable to the magnetic moments of bulk hcp Co ($1.7 \mu_B$) and fcc Ni ($0.6 \mu_B$) [97,98], justifying our choice of $U = 1$ eV. For the relaxation of the heterostructures, we add van der Waals corrections [99,100] and use a quasi-Newton algorithm based on trust radius procedure. In order to simulate quasi-2D systems, a vacuum of at least 16 \AA is used to avoid interactions between periodic images in our slab geometries. Dipole corrections [101] are included for heterostructure calculations to get correct band offsets and internal electric fields. Structural relaxations are performed until all components of all forces were reduced below 10^{-3} (Ry/ a_0), where a_0 is the Bohr radius.

B. Absorption spectra calculations for excitons

To compute the excitonic spectra, we employ the effective Bethe-Salpeter equation (BSE) [62,102–107] focusing on direct intralayer excitons at zero temperature and without doping effects. The specific form of the BSE we use is given in the Supplemental Material of Ref. [62]. The single-particle spectra is obtained using the model Hamiltonian of Eq. (1) fitted to the first-principles band structures. Because of the coupling between conduction and valence band states (due to the Fermi velocity term), the direct term of the electron-hole interaction is given by

$$\mathbb{D}_{c'v'\vec{k}'}^{cv\vec{k}} = -\Delta_{c'v'\vec{k}'}^{cv\vec{k}} V(\vec{k} - \vec{k}'), \quad (7)$$

with $V(\vec{k} - \vec{k}')$ being the electrostatic potential and the mixing term $\Delta_{c'v'\vec{k}'}^{cv\vec{k}}$ can be written in a very general way as

$$\Delta_{c'v'\vec{k}'}^{cv\vec{k}} = \left[\sum_l^M \beta_{c,l}(\vec{k}) \beta_{c',l}(\vec{k}') \right] \left[\sum_m^M \beta_{v',m}^*(\vec{k}') \beta_{v,m}(\vec{k}) \right], \quad (8)$$

in which M is the size of the effective Hamiltonian, c, c' (v, v') are the conduction (valence) bands, and $\beta_{n,l}(\vec{k})$ is the l th coefficient ($l = 1, \dots, M$) of the band n at point \vec{k} . We point out that for decoupled models, for instance parabolic dispersions described by effective masses, the mixing term (8) would not be present and the BSE is reduced to the Wannier equation in k space [108].

We model the electron-hole electrostatic potential $V(\vec{k} - \vec{k}')$ that appears in Eq. (7) by the widely used Rytova-Keldysh potential [109–114]. Such potential essentially describes the electrostatics of a thin slab, i.e., the 2D material, with different top and bottom dielectric environments. In k space the Rytova-Keldysh potential is given by

$$V(\vec{K}) = \frac{1}{\mathcal{A}} \frac{e^2}{2\varepsilon_0 \varepsilon K + r_0 K^2}, \quad (9)$$

with $\vec{K} = \vec{k} - \vec{k}'$, \mathcal{A} is the 2D unit area, e is the electron charge, ε_0 is the vacuum permittivity, r_0 is the screening length of the 2D material, and ε is the effective dielectric constant given by the average of the top and bottom dielectric constants, i.e., $\varepsilon = (\varepsilon_t + \varepsilon_b)/2$. For the screening lengths of the TMDCs we used the values provided in Ref. [112].

The BSE is solved on a 2D k grid from -0.5 to 0.5 \AA^{-1} in k_x and k_y directions with total discretization of 101×101 points (leading to a spacing of $\Delta k = 10^{-2} \text{ \AA}^{-1}$). To improve convergence, the Coulomb potential is averaged around each k point in a square region of $-\Delta k/2$ to $\Delta k/2$ discretized with 101×101 points [62,105].

The absorption spectra for a photon with energy $\hbar\omega$, incorporating excitonic effects, is given by [105,106]

$$\alpha^a(\hbar\omega) = \frac{4\pi^2 e^2}{\varepsilon_0 c_l \omega \mathcal{A} \hbar^2} \sum_N \left| \sum_{cv\vec{k}} A_{cv\vec{k}}(N) p_{vc}^a(\vec{k}) \right|^2 \delta(\Omega_N - \hbar\omega), \quad (10)$$

with the superindex a indicating the polarization of the light, e is the electron charge, ε_0 is the vacuum permittivity, c_l is the speed of light (the subindex l was added to not be confused with the conduction band index c), \mathcal{A} is the 2D unit area, the summation indices c and v label the conduction and valence bands, respectively, \vec{k} is the wave vector, N labels the excitonic states, $A_{cv\vec{k}}(N)$ is the exciton envelope function, Ω_N is the exciton energy, and the single-particle dipole matrix element is $p_{mm}^a(\vec{k}) = \frac{\hbar}{m_0} \langle n, \vec{k} | \hat{e}_a \cdot \vec{p} | m, \vec{k} \rangle$ (computed using the eigenstates of the model Hamiltonian). Finally, to the calculated absorption spectra we apply a Lorentzian broadening with energy dependent full width at half-maximum [106,115]

$$\Gamma(\hbar\omega) = \Gamma_1 + \frac{\Gamma_2}{1 + e^{[(E_0 - \hbar\omega)/\Gamma_3]}} \quad (11)$$

using $\Gamma_1 = \Gamma_2 = \Gamma_3 = 10$ meV. E_0 is the single-particle energy at the K point for the first allowed optical transition.

IV. TMDC/hBN/FM HETEROSTRUCTURES

A. Geometry

In order to calculate the proximity exchange in a TMDC/hBN/FM heterostructure, we have to find a common unit cell for all compounds minimizing strain effects. In Fig. 1 we show the geometry for MoS₂/hBN/Co as an exemplary structure. Initial atomic structures are set up with the atomic simulation environment (ASE) [116], as follows. We choose a 4×4 supercell of the TMDC (MoS₂, WS₂), a 5×5 cell of hBN, and a 5×5 cell of the FMs (Co, Ni). For the FM we take three monolayers of hcp Co or fcc(111) Ni. The hBN is placed above the FM, such that the nitrogen sits above the topmost Co/Ni atom, and the boron above the fcc position above the FM slab, as found by previous studies [19]. The TMDC is placed above the hBN/FM slab, that a transition metal atom (Mo, W) sits above a nitrogen atom. By choosing the heterostructure as explained, our unit cell contains 173 atoms, with a lattice constant of $a = 12.637 \text{ \AA}$, for all of our considered hybrid geometries. For that we have to modify the lattice constants of the subsystem layers (TMDC, hBN, FM). In Table I we give an overview on the original experimental and the new modified lattice constants used for the heterostructures, as well as the introduced strain. We can see that a maximum strain of about 1.5% is present for Ni, being still acceptable for our purposes.

To determine the interlayer distances, the atoms of the TMDC, hBN, and the top two Co/Ni layer atoms were

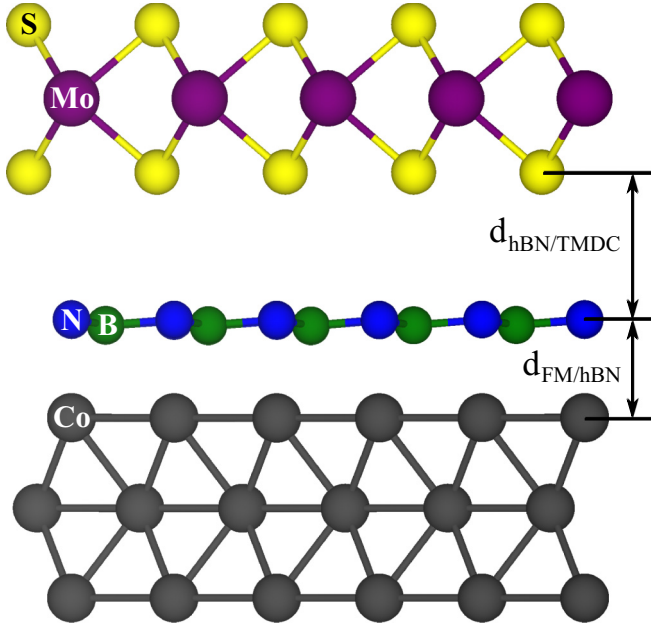


FIG. 1. Side view of the TMDC/*h*BN/FM structure with labels for the atoms and distances. As an example, we show here MoS₂/*h*BN/Co. The distances between the layers $d_{\text{FM}/\text{hBN}}$ and $d_{\text{hBN}/\text{TMDC}}$ are listed in Table III for all considered heterostructures.

allowed to relax only in their z positions (vertical to the layers). The average distances between the layers $d_{\text{FM}/\text{hBN}}$ and $d_{\text{hBN}/\text{TMDC}}$, as defined in Fig. 1, are listed in Table III for all considered geometries. The distances are measured from the average position of the top Co/Ni (bottom S) atoms, with respect to the average position of the N atoms of the *h*BN layer. The corrugation of the *h*BN is on average 0.12 Å, independent of the heterostructure. The distances $d_{\text{FM}/\text{hBN}}$ between the FMs and *h*BN are around 2.1 Å, indicating strong bonding. The distances $d_{\text{hBN}/\text{TMDC}}$ between the *h*BN and the TMDCs are roughly 3.15 Å, being in the range of typical van der Waals distances. All these observations are in agreement with previous calculations of *h*BN on metallic substrates [19,122,123], as well as TMDCs on *h*BN/metal interfaces [65,66].

In Table II we summarize the calculated averaged atomic magnetic moments. For example, in the case of MoS₂/*h*BN/Co, we find that the average magnetic moments in the first, second, and third Co layer are 1.77, 1.71, and

TABLE I. Overview of the lattice constants and strains for the subsystems used in the TMDC/*h*BN/FM heterostructures. The experimental a (expt) lattice constants [117–121] of the bulk systems and lattice constants used for the heterostructures a (het) are given, along with the introduced strain for each subsystem, calculated as $(a_{\text{het}} - a_{\text{expt}})/a_{\text{expt}}$. Note that for nickel it is the lattice constant of a fcc(111) quasi-hexagonal surface.

	Co	Ni	<i>h</i> BN	MoS ₂	WS ₂
a (expt) (Å)	2.507	2.492	2.504	3.150	3.153
a (het) (Å)	2.527	2.527	2.527	3.159	3.159
Strain (%)	0.8	1.4	0.9	0.3	0.2

TABLE II. Calculated atomic magnetic moments of the TMDC/*h*BN/FM systems given in μ_B . The values are obtained by averaging the magnetic moments of the individual atomic species. For Co/Ni atoms we distinguish the three layers of the FM slab by the numbers in brackets (1–3) ordered from vacuum to *h*BN-interface side.

System	MoS ₂	MoS ₂	WS ₂	WS ₂
	<i>h</i> BN	<i>h</i> BN	<i>h</i> BN	<i>h</i> BN
	Co	Ni	Co	Ni
Mo/W	0.004	0.003	0.002	0.002
B	−0.010	−0.004	−0.010	−0.004
N	0.003	0.014	0.003	0.014
Co/Ni (3)	1.60	0.61	1.60	0.61
Co/Ni (2)	1.71	0.76	1.71	0.76
Co/Ni (1)	1.77	0.75	1.77	0.75

1.60 μ_B , ordered from vacuum to the *h*BN interface. The FM metal layer induces a small negative (positive) magnetic moment in the B (N) atoms of about −0.010 (0.003) μ_B . In the case of Ni, the magnitude of proximity induced magnetic moments in the *h*BN layer are different compared to Co. Due to the different lattices and magnetic moments of fcc(111) Ni and hcp Co, the hybridization of FM d orbitals and *h*BN p orbitals and the resulting proximity exchange strength are not completely the same in the two cases. Finally, the Mo atoms have a magnetic moment of about 0.004 μ_B , which is responsible for the exchange splitting in the TMDC bands, which we analyze in the following.

B. Band structure analysis and fit results

In the following we analyze the results for MoS₂/*h*BN/Co, shown in Fig. 2, as a representative example. Similar to Fig. 2, we show the DFT results for the other TMDC/*h*BN/FM heterostructures in the Appendix.

In Fig. 2(a) we show the calculated band structure without SOC of the MoS₂/*h*BN/Co heterostructure. Since a lot of bands are involved, originating from the *h*BN/FM substrate,

TABLE III. Summary of the fit parameters, calculated dipoles, and distances for TMDC/*h*BN/FM systems without SOC. The Hamiltonian used to fit these systems is $\mathcal{H}_0 + \mathcal{H}_\Delta + \mathcal{H}_{\text{ex}}$, with Δ as the orbital gap of the spectrum, the Fermi velocity v_F , and B_c and B_v are the proximity exchange parameters, respectively. The dipole of the structures is given in debye and $d_{\text{hBN}/\text{TMDC}}$ is the distance between *h*BN and the TMDC, and $d_{\text{FM}/\text{hBN}}$ is the distance between the FM and *h*BN, as defined in Fig. 1.

System	MoS ₂	MoS ₂	WS ₂	WS ₂
	<i>h</i> BN	<i>h</i> BN	<i>h</i> BN	<i>h</i> BN
	Co	Ni	Co	Ni
Δ (eV)	1.761	1.769	1.910	1.910
v_F ($10^5 \frac{\text{m}}{\text{s}}$)	5.303	5.475	6.907	6.908
B_c (meV)	1.964	1.697	1.080	1.077
B_v (meV)	6.365	2.185	3.629	2.308
Dipole (Debye)	1.940	2.871	2.386	3.713
$d_{\text{FM}/\text{hBN}}$ (Å)	2.089	2.085	2.089	2.084
$d_{\text{hBN}/\text{TMDC}}$ (Å)	3.157	3.217	3.151	3.137

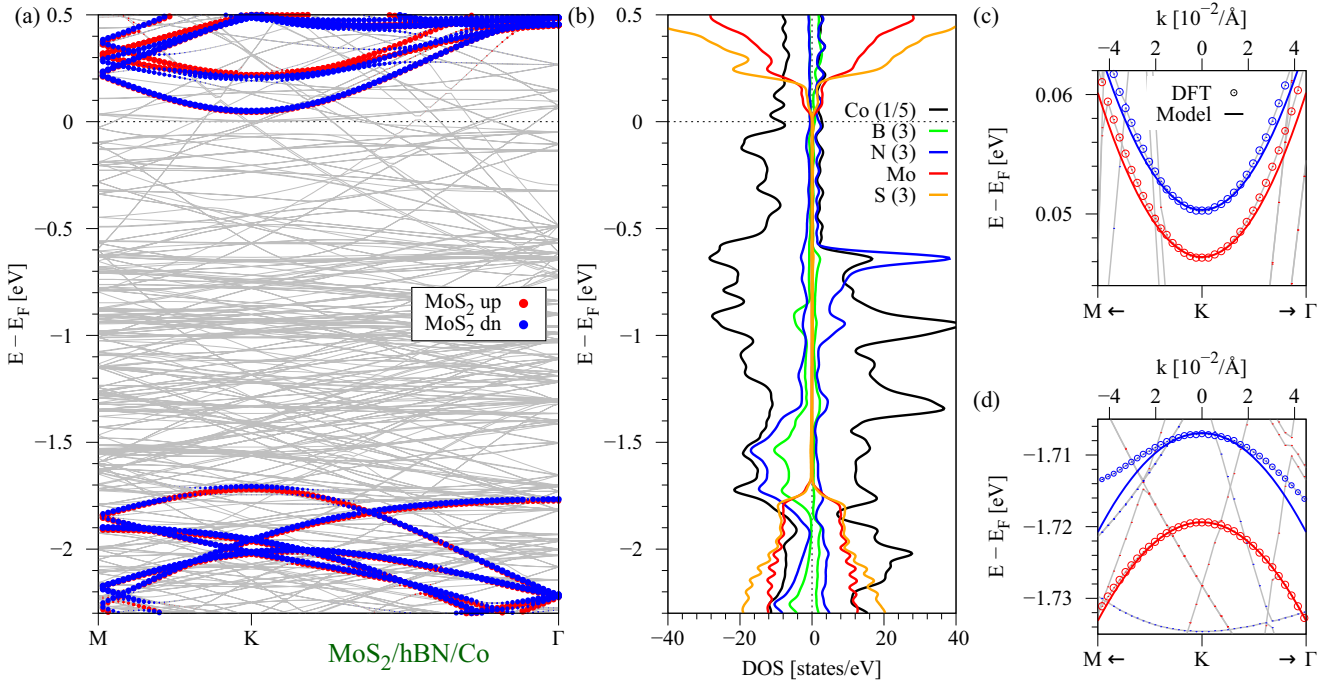


FIG. 2. Calculated band structure and density of states of the MoS₂/hBN/Co system without SOC. (a) Band structure along high symmetry path M - K - Γ . The bands corresponding to MoS₂ are emphasized by red (spin up) and blue (spin down) spheres. Bands originating from the hBN/Co substrate are plotted in gray. (b) The atom and spin resolved density of states of the heterostructure, where different colors correspond to different atoms. The number in brackets is the multiplication factor, i.e., the contribution of, for example, B atoms is multiplied by a factor of 3. (c) Zoom to the CB edge originating from MoS₂ around the K point. Symbols are DFT data and solid lines are the fit to the model Hamiltonian. (d) Same as (b), but for VB edge.

we only show a projection of the bands originating from the TMDC. We find that the band structure closely resembles the bands of pristine MoS₂. The Fermi level is located below the TMDC CB edge. Our calculated band structure is very different compared to other studies of proximity induced exchange [55–57], where the TMDC experiences strong doping, probably due to the polar surfaces of the substrates they consider. Note that a polar surface does not reflect a realistic situation, as surface reconstructions are present in real experiments. This can strongly modify the proximity exchange in experiments, as the hybridization with the substrate is the main origin of proximity exchange. Such effects are absent in a hBN/FM hybrid substrate, due to the hBN buffer layer. Another advantage of our FM/hBN substrate is that the Curie temperature of the standard ferromagnets [118] Co ($T_C = 1388$ K) and Ni ($T_C = 627$ K) is well above room temperature, allowing for experiments at ambient conditions. The ultimate goal is the spin injection into the TMDC via the hBN/FM tunnel junction.

In Fig. 2(b) we show the atom and spin resolved density of states of the MoS₂/hBN/Co heterostructure. In the chosen energy window around the Fermi level, mainly the Co atoms contribute to the density of states. We also find that hBN is not an insulator anymore, as states from the N and B atoms are present in the whole energy range. Note that the actual band edges of the hBN do not reside within the shown energy window. Especially interesting is the relatively large contribution of N spin-up (spin-down) states at about -0.65 (-1.7) eV below the Fermi level, which is an indication of strong hybridization with the FM layers. More precisely, the

Co d orbitals hybridize with the p orbitals of the hBN layer and mediate the exchange coupling. The band edges of the MoS₂ layer can be also identified in the density of states at about 0 and -1.7 eV. Especially near the VB edge of MoS₂ at around -1.7 eV, there is a significant contribution from B and N atoms in the spin-down channel. Thus, the Co d orbitals hybridize, via the hBN buffer layer, with the VB spin-down states of MoS₂.

If we zoom to the fine structure around the K point, we find that the bands of the TMDC are spin split due to proximity exchange coupling, see Figs. 2(c) and 2(d). The splitting of the CB is smaller than that of the VB, both being in the few meV range. Since SOC effects are turned off, we can fit the band structure around the K point to our model Hamiltonian, neglecting for now $\mathcal{H}_{\text{soc}} + \mathcal{H}_R$. In Figs. 2(c) and 2(d) we can see that the bands are nicely reproduced by the model with the fit parameters given in Table III. However, we can see that there is a discrepancy between the model and the calculation, especially for the spin-down VB away from the K point. The case of MoS₂/hBN/Co is the only one, where this happens. The origin of this, is the hybridization of the VB spin-down states of MoS₂ with Co d states, as one can see in Figs. 2(a) and 2(b).

In Table III we summarize our fit parameters for all considered heterostructures. We notice that especially the parameter B_v for the MoS₂/hBN/Co case is very large, which is caused by the previously explained effect of hybridization. In a similar way, an earlier study has shown that the hybridization with Co d orbitals can strongly enhance the proximity exchange splitting in graphene on a hBN/Co substrate [19]. Note that

TABLE IV. Summary of the fit parameters, calculated dipoles, and distances for TMDC/*h*BN systems with SOC. The Hamiltonian used to fit these systems is $\mathcal{H}_0 + \mathcal{H}_\Delta + \mathcal{H}_{\text{soc}} + \mathcal{H}_R$, with Δ as the orbital gap of the spectrum, the Fermi velocity v_F , and λ_c and λ_v are the SOC parameters. The distances are given as defined in Fig. 1.

System	MoS ₂ <i>h</i> BN	WS ₂ <i>h</i> BN
Δ (eV)	1.756	1.872
v_F ($10^5 \frac{\text{m}}{\text{s}}$)	5.432	6.786
λ_c (meV)	-1.361	17.03
λ_v (meV)	72.96	208.6
Dipole (Debye)	-0.701	-0.703
$d_{h\text{BN}/\text{TMDC}}$ (Å)	3.330	3.252

the value of the Hubbard U , which shifts the Co d levels in energy, affects the hybridization and the spin splitting, as shown in Ref. [19]. Since we have considered $U = 1$ eV only, we can only predict that such a hybridization is present in experiments, which leads to an enhanced spin splitting.

Unfortunately, we were not able to properly converge the calculations of the TMDC/*h*BN/FM heterostructures including SOC effects. The spin-orbit splitting in the TMDC VB is large [38,124] and may shift the corresponding bands too much in energy to spoil the hybridization. Therefore, we cannot be completely sure whether the mentioned hybridization effect in the MoS₂/*h*BN/Co structure will remain. However, a similar work of proximity exchange in TMDC/CrI₃ heterostructures has shown that inclusion of SOC barely affects the proximity exchange parameters [62]. Thus, we believe that proximity exchange on the order of 1–5 meV would still be present when including SOC for our TMDC/*h*BN/FM structures.

Similar to graphene/*h*BN/FM stacks [19], we expect that the proximity exchange in the TMDCs also decreases with increasing number of *h*BN layers between the FM and the TMDC. Unfortunately, due to computational limitations (number of atoms in the supercell), we cannot study more than one *h*BN layer.

C. TMDC/*h*BN subsystems

Experimentally it is also interesting to consider the bare MoS₂/*h*BN and WS₂/*h*BN heterostructures, without any influence from the FM. For that we take the TMDC/*h*BN/FM geometries, but remove the FM layers. After subsequent relaxation, similar as described above, we calculate the electronic band structures for the *subsystems*, including SOC effects. The corrugation of the *h*BN reduces to about 20 pm on average, and the distances $d_{h\text{BN}/\text{TMDC}}$ between *h*BN and the TMDC are given in Table IV for the TMDC/*h*BN stacks. The FM is responsible for the corrugation of the *h*BN layer, as already pointed out in an earlier work [19]. Our model Hamiltonian is also suitable to describe this situation, when neglecting \mathcal{H}_{ex} .

The calculated band structure for MoS₂/*h*BN is shown in Fig. 3. We find that we can perfectly reproduce the band structure around K and K' valleys, with the fit parameters given in Table IV. The fit parameters for the TMDC/*h*BN

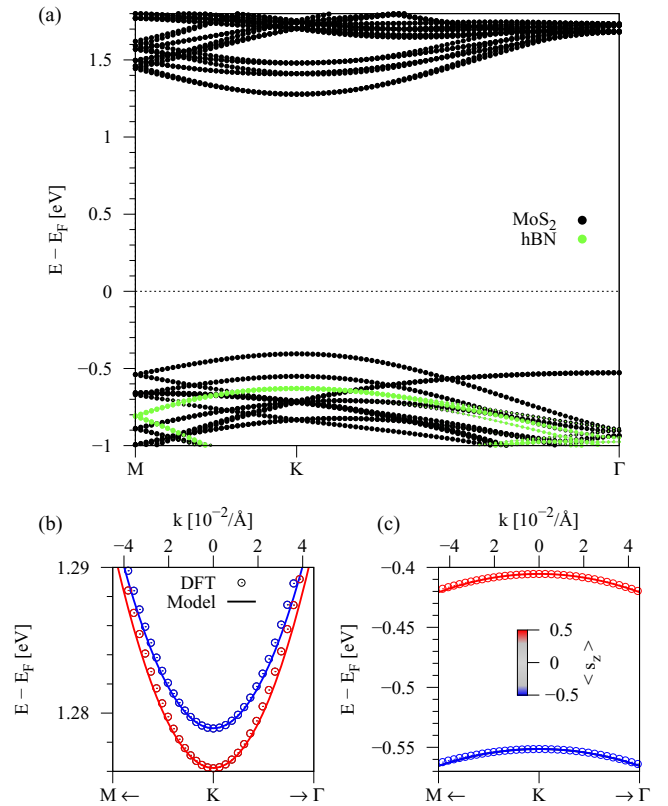


FIG. 3. Calculated band structure of MoS₂/*h*BN including SOC effects. (a) Band structure along high symmetry lines. The bands corresponding to MoS₂ (*h*BN) are plotted in black (green). (b) Zoom to the CB edge. The color corresponds to the s_z -expectation value. Symbols are DFT data and solid lines are fits to the model Hamiltonian. (c) Same as (b), but for VB edge.

heterostructures are nearly identical to the ones obtained for the bare TMDC monolayers [38,124]. We conclude that the *h*BN has effectively no impact on the TMDC dispersion and SOC. In principle, one would also expect Rashba SOC due to inversion symmetry breaking, but from previous calculations of graphene/*h*BN/FM structures [19], we conclude that the proximity induced SOC due to the *h*BN/FM substrate is negligible, compared to the proximity induced exchange and the giant intrinsic SOC of the bare TMDCs [38,124]. Indeed, we find by fitting the model Hamiltonian to the band structure of the TMDC/*h*BN systems, that \mathcal{H}_R can be neglected, as the s_z spin expectation values of the bands near the K and K' points almost do not differ from ± 0.5 , as we can see in Fig. 3.

In conclusion, the extracted proximity exchange (intrinsic SOC) parameters from the calculations of the TMDC/*h*BN/FM (TMDC/*h*BN) systems, together with the Hamiltonian, can be used for further studies.

V. PROXIMITY EXCHANGE INDUCED VALLEY SPLITTING

The individually extracted parameters for proximity exchange and SOC, see Tables III and IV, in combination with our model Hamiltonian, can be used to calculate the low energy bands around K and K' point with both effects present. We average the parameters for v_F and Δ from Tables III

TABLE V. Summary of the model Hamiltonian parameters, combined from Tables III and IV. The orbital gap parameter Δ , the Fermi velocity v_F , B_c and B_v are the proximity exchange parameters, and λ_c and λ_v are the SOC parameters. The valley splitting calculated from the single particle picture (s. part.) and from the absorption spectra of the A_{1s} exciton peak.

System	MoS ₂	MoS ₂	WS ₂	WS ₂
	<i>h</i> BN Co	<i>h</i> BN Ni	<i>h</i> BN Co	<i>h</i> BN Ni
Δ (eV)	1.759	1.763	1.891	1.891
v_F ($10^5 \frac{m}{s}$)	5.368	5.454	6.847	6.847
λ_c (meV)	-1.361	-1.361	17.03	17.03
λ_v (meV)	72.96	72.96	208.6	208.6
B_c (meV)	1.964	1.697	1.080	1.077
B_v (meV)	6.365	2.185	3.629	2.308
s. p. at K, K' (meV)	8.80	0.98	5.10	2.46
A_{1s} ($\epsilon = 2.75$) (meV)	8.20	0.91	4.76	2.30
A_{1s} ($\epsilon = 4.5$) (meV)	8.31	0.93	4.84	2.34

and IV, for the MoS₂ and WS₂ based structures. We take the SOC parameters for the two TMDCs from Table IV, and the proximity exchange parameters from Table III. The full parameter sets are summarized in Table V, which we use for the following absorption spectra calculations.

In this context, one can also generalize the exchange Hamiltonian [55] to $\mathcal{H}_{ex} = -\hat{\mathbf{m}} \cdot \mathbf{s} \otimes (B_c \sigma_+ + B_v \sigma_-)$, with $\hat{\mathbf{m}}$ being a unit vector for the direction of the proximity exchange field and \mathbf{s} is the vector containing Pauli spin matrices. In Fig. 4 we show the calculated model band structure employing the full Hamiltonian with SOC and proximity exchange, setting $\hat{\mathbf{m}} = \hat{m}_z$, for the MoS₂/*h*BN/Co heterostructure, using the parameters from Table V. Due to the combination of SOC

and proximity exchange, time-reversal symmetry is broken and the valley degeneracy is lifted, as can be seen when comparing the spin-split CB at K and K' , see Figs. 4(a) and 4(c). Remarkably, the order of the spin bands in the CB is the same for the two valleys. For bare TMDCs, the spin splitting in the CB is determined by the corresponding SOC parameter λ_c . For the case of MoS₂, we find that the SOC parameter is comparable in magnitude with the proximity exchange parameter $\lambda_c \approx B_c$, due to the *h*BN/FM substrate. When the proximity exchange is larger than the SOC, the band ordering of the spin-split CB is the same for both valleys, as can be seen in Figs. 4(a) and 4(c). In contrast, the VB SOC parameter is much larger than the corresponding proximity exchange parameter $\lambda_v \gg B_v$, and the VB splitting is dominated by SOC.

For a more realistic assessment of the proximity exchange in the optical spectra, we investigate the valley splitting of the excitonic levels, employing the parameters summarized in Table V for the model Hamiltonian and the effective BSE. Let us first look at the absorption spectra assuming an effective dielectric constant of $\epsilon = 2.75$ as a model case of a TMDC placed on *h*BN ($\epsilon_b = 4.5$ [125]) and vacuum on top ($\epsilon_t = 1$), as suggested by the geometry shown in Fig. 1. The calculated absorption spectra for the TMDC intralayer excitons is shown in Fig. 5 as function of the photon energy E_{ph} relative to the optical energy gap at the K point, E_K (the energy of the first allowed optical transition). With this x -axis convention, the energy of the first absorption peak is roughly the A_{1s} exciton binding energy. Because we are assuming a TMDC embedded in a dielectric environment with effective $\epsilon = 2.75$, the exciton binding energy is smaller than in the freestanding case (with $\epsilon = 1$ the binding energies are typically 0.5–0.6 eV for TMDCs [112,126]). Due to the induced proximity exchange, K and K' valleys have now different transition energies and this is directly reflected in the absorption spectra as a splitting of the excitation energies with σ_+ and σ_- polarizations. The extracted values for the valley splitting of the A_{1s} exciton peak and for the single-particle picture at the K, K' points are summarized in Table V. Along with the visible excited excitonic states A_{2s} and A_{3s} , the B excitons are also visible for the MoS₂-based systems. For instance, B_{1s} excitons show large peaks around -150 meV and have a valley splitting with the same value as the A_{1s} exciton but with opposite sign.

What about the valley splitting of other exciton peaks and the effect of stronger dielectric surroundings? In Figs. 6(a)–6(d) we show the valley splittings of the A excitons ($1s$, $2s$, and $3s$) visible in Fig. 5 for effective dielectric constants of $\epsilon = 2.75$ and $\epsilon = 4.5$ (resembling a case for *h*BN encapsulated TMDC or assuming a stronger screening due to the presence of Co/Ni below the *h*BN layer [127]). Essentially, excited excitonic states and larger values of ϵ provide larger valley splittings which tend to converge to the single-particle values obtained directly at the K, K' points. In order to grasp the physics behind this behavior, we can look at the expectation value of the exciton valley splitting given by $\langle A_{\vec{k}}^K | E_K(\vec{k}) | A_{\vec{k}}^K \rangle - \langle A_{\vec{k}}^{K'} | E_{K'}(\vec{k}) | A_{\vec{k}}^{K'} \rangle$. Since the exciton wave functions are nearly identical for K and K' points (due to same effective masses) we can simply write the expectation

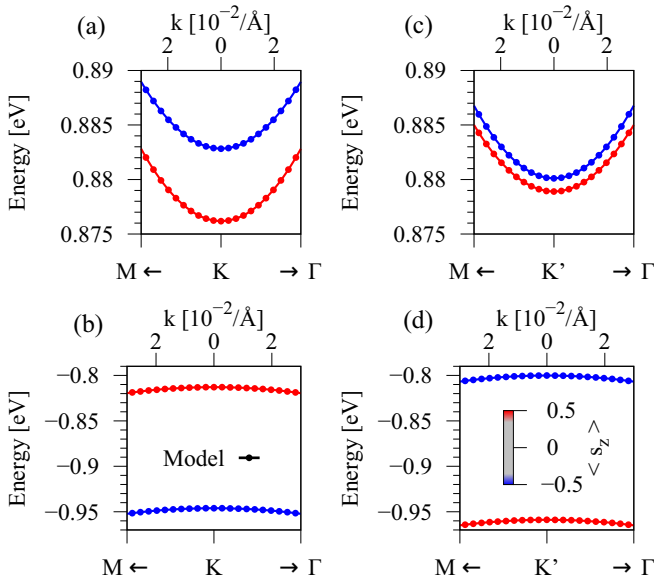


FIG. 4. Calculated model band structure employing the full Hamiltonian, for MoS₂/*h*BN/Co heterostructure using parameters from Table V. (a) and (b) Low energy CB and VB at the K point. (c) and (d) Same as (a) and (b) but for the K' point.

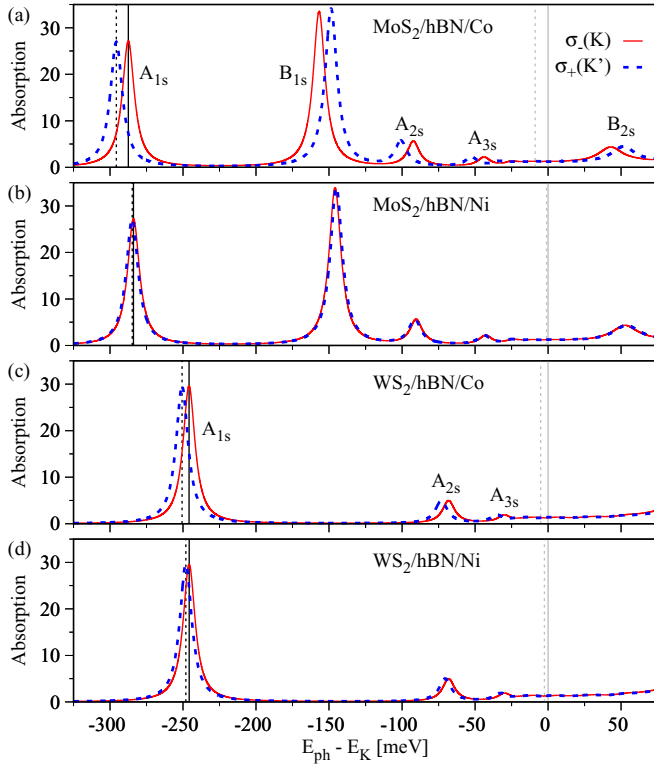


FIG. 5. Calculated absorption spectra for (a) $\text{MoS}_2/\text{hBN}/\text{Co}$, (b) $\text{MoS}_2/\text{hBN}/\text{Ni}$, (c) $\text{WS}_2/\text{hBN}/\text{Co}$, and (d) $\text{WS}_2/\text{hBN}/\text{Ni}$. In the x axis, E_{ph} is the photon energy ($\hbar\omega$) and E_K is the optical energy gap at the K point. The vertical solid (dashed) lines indicate the energy gap contribution at the K (K') point. The vertical lines close to $E_{\text{ph}} - E_K = 0$ indicate the single-particle energies while the vertical lines at the A_{1s} exciton peaks indicate the excitonic contribution. The energy difference between σ_+ and σ_- polarizations is the valley splitting, summarized in Table V. Additional exciton peaks are also labeled. For these calculations we considered an effective dielectric constant of $\varepsilon = 2.75$.

value of the valley splitting as $\langle A_{\vec{k}} | \Delta(\vec{k}) | A_{\vec{k}} \rangle$, in which $\Delta(\vec{k}) = E_K(\vec{k}) - E_{K'}(\vec{k})$ is the single-particle valley splitting in momentum space. The spreading of $\Delta(\vec{k})$ (calculated with the model Hamiltonian) and the exciton envelope functions are shown in Figs. 6(e)–6(h). Since $\Delta(\vec{k})$ has a maximum value at $\vec{k} = 0$, the largest exciton valley splitting in this case is achieved for excitons more localized at $\vec{k} = 0$, which is precisely the effect of looking at excited exciton states or increasing the effective dielectric constant as shown in Figs. 6(a)–6(d). This intuitive picture of looking at the expectation value within the exciton framework has been recently employed to successfully explain the evolution of the g factor in excited exciton states [128]. Furthermore, our analysis suggests that one possibility to engineer larger exciton valley splittings is to look for proximity exchange effects that increase as one moves away of the K, K' edges.

As a final remark, we point out that the optical excitation energy difference between K and K' valleys for $\text{MoS}_2/\text{hBN}/\text{Co}$ is giant, around 8 meV, translating into about 50 T magnetic field for bare TMDCs, if assuming 0.15 meV/T valley splitting [49–52]. A similar giant valley splitting of

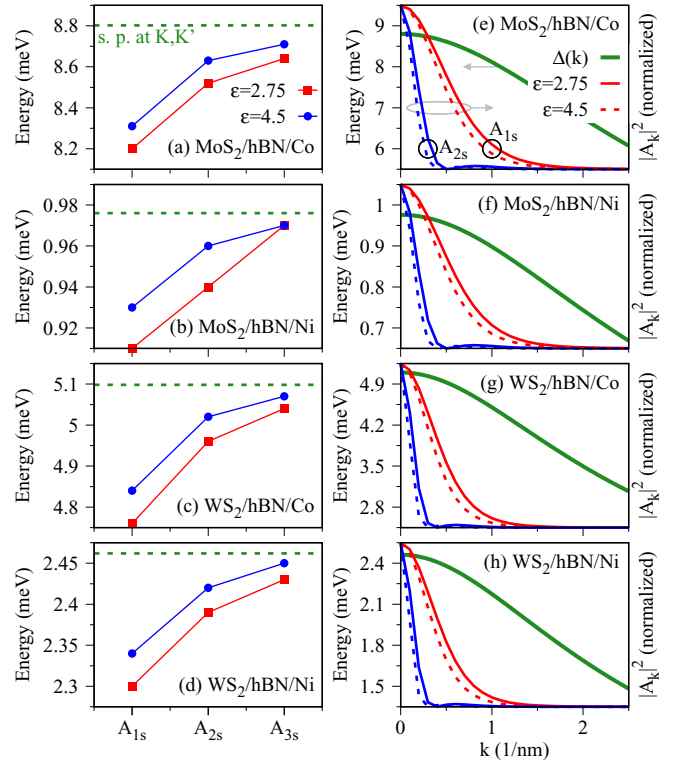
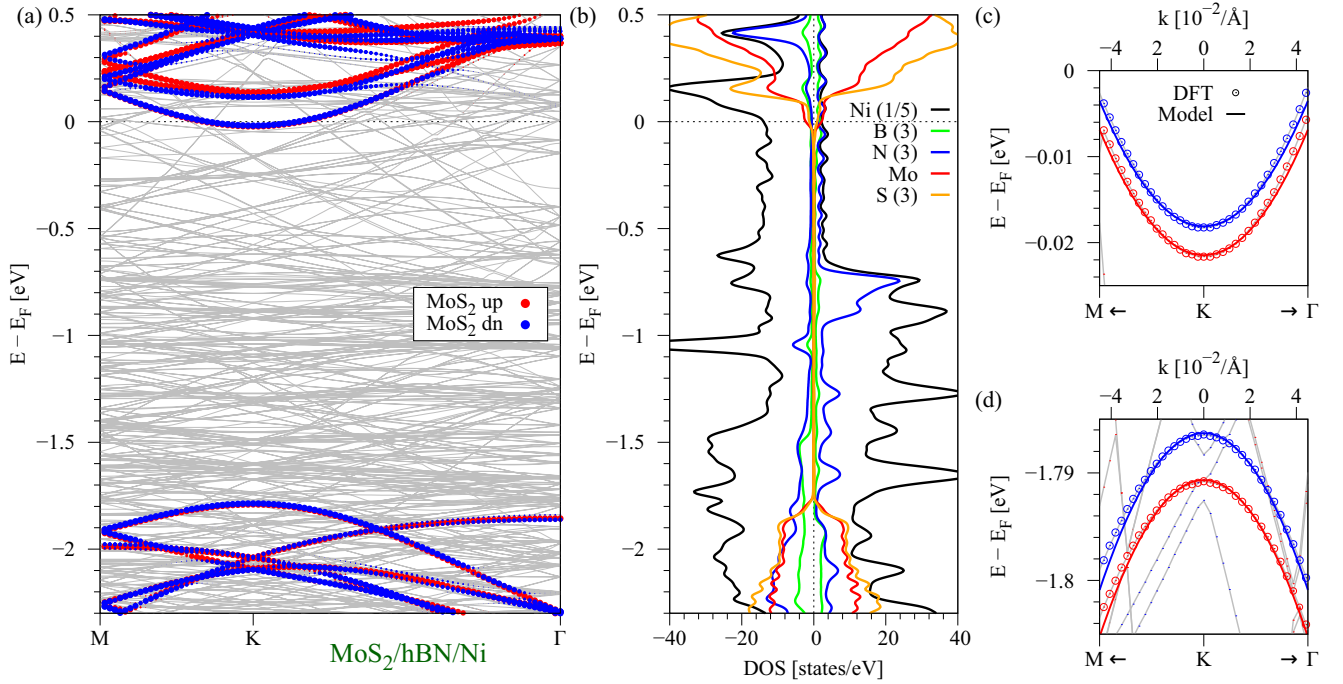


FIG. 6. Valley splitting of the A_{1s} , A_{2s} , and A_{3s} excitons in distinct dielectric surroundings, $\varepsilon = 2.75$ and $\varepsilon = 4.5$, for (a) $\text{MoS}_2/\text{hBN}/\text{Co}$, (b) $\text{MoS}_2/\text{hBN}/\text{Ni}$, (c) $\text{WS}_2/\text{hBN}/\text{Co}$, and (d) $\text{WS}_2/\text{hBN}/\text{Ni}$. The horizontal dashed line is the single-particle valley splitting directly at K, K' (with values given in Table V). The valley splitting for different excitons and dielectric surroundings can be understood by looking at the spreading in momentum space of the single-particle valley splitting $\Delta(\vec{k}) = E_K(\vec{k}) - E_{K'}(\vec{k})$ (y axis on the left side of the plot) and the exciton wave function (y axis on the right side of the plot) for (e) $\text{MoS}_2/\text{hBN}/\text{Co}$, (f) $\text{MoS}_2/\text{hBN}/\text{Ni}$, (g) $\text{WS}_2/\text{hBN}/\text{Co}$, and (h) $\text{WS}_2/\text{hBN}/\text{Ni}$. In the x axis, $k = 0$ is at the K, K' points. The exciton wave functions are scaled to have the same value at $k = 0$.

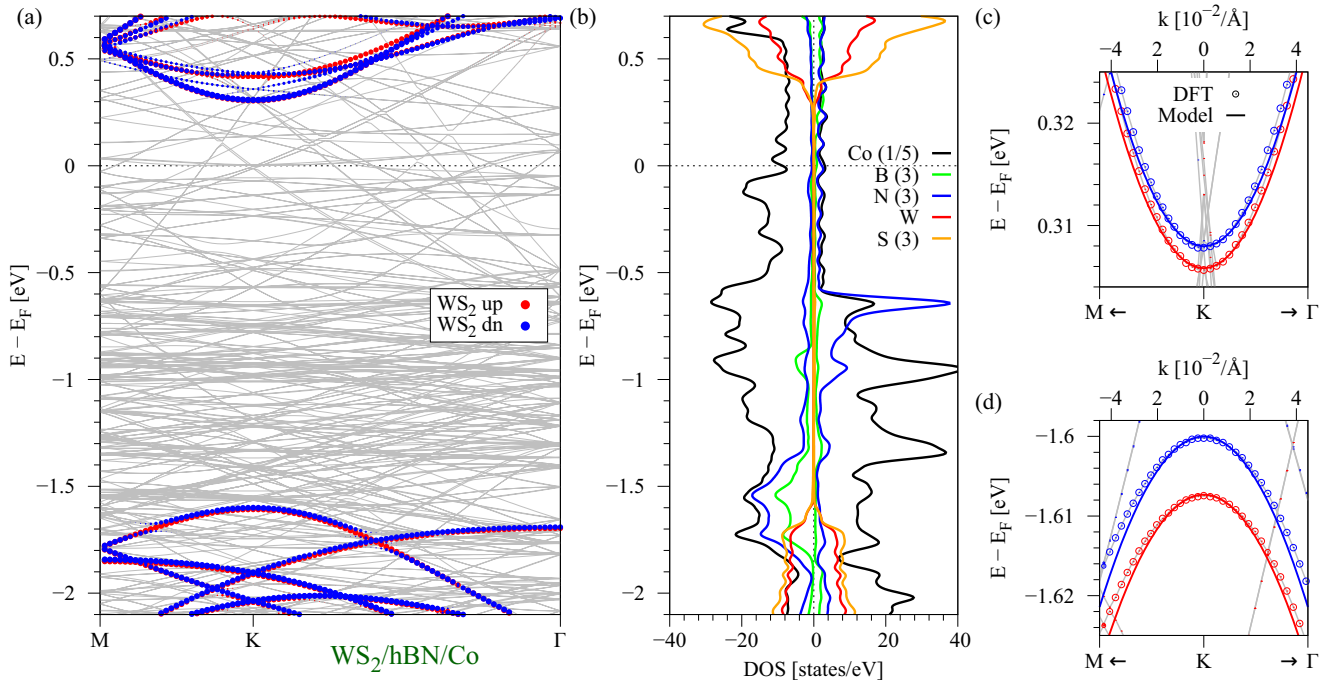
about 5 meV is achieved in the case of $\text{WS}_2/\text{hBN}/\text{Co}$, translating to about 30 T magnetic field. Remarkably, in the case of $\text{MoS}_2/\text{hBN}/\text{Co}$, we have seen that proximity exchange together with band hybridization to d orbitals causes a large VB splitting, leading to the giant valley splitting. In the case of $\text{WS}_2/\text{hBN}/\text{Co}$, the valley splitting is also giant, but without any band hybridization effects. When Ni is considered as the FM, we find smaller valley splittings, ~ 1 meV (7 T) for $\text{MoS}_2/\text{hBN}/\text{Ni}$ and 2.3 meV (15 T) for $\text{WS}_2/\text{hBN}/\text{Ni}$, but still the corresponding magnetic fields are quite large, compared to the valley splittings achieved without proximity exchange. Furthermore, our exciton calculations show that the valley splitting increases for excited exciton states, which could be observed experimentally in reflectance/transmittance measurements [113,125]. Besides a direct observation of the exciton valley splitting, recent studies have shown that the induced proximity exchange has visible signatures in the magneto-optical Kerr response of excitons [129,130].

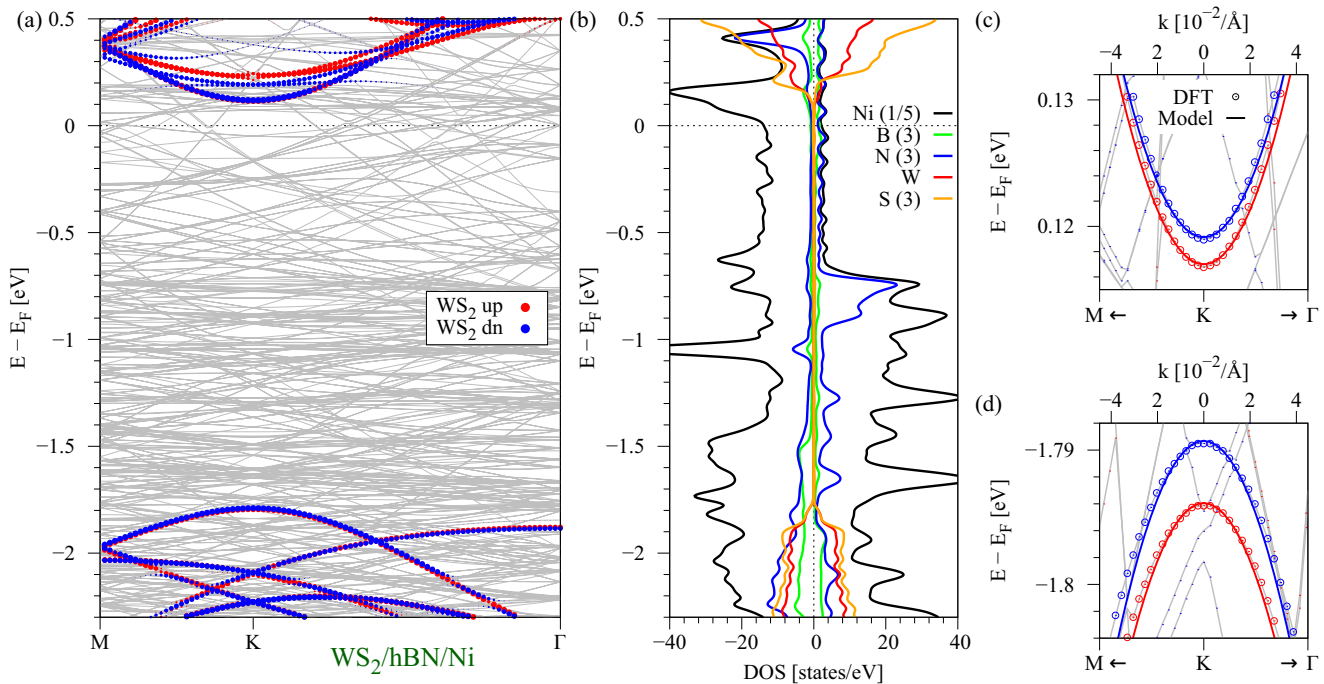
FIG. 7. Same as Fig. 2, but for the MoS₂/hBN/Ni system.

VI. SUMMARY

We have calculated the band structures of TMDC/hBN/FM heterostructures and extracted valuable proximity exchange and SOC parameters, using a minimal low energy Hamiltonian. Due to the hBN buffer layer, the TMDC preserves a great degree of autonomy of its electronic structure. Proximity exchange is found to be on the order of 1–10 meV,

depending on the specific FM. Especially in MoS₂/hBN/Co, the spin splitting is giant, about 10 meV, due to proximity exchange and hybridization of Co *d* states with the spin-down VB of the TMDC. The excitonic absorption spectra, shows a giant valley splitting for the exciton peaks, translating into a valley polarization corresponding to tens of Tesla exchange field for bare TMDC monolayers. The Ni-based heterostructures show less strong proximity exchange. We believe our

FIG. 8. Same as Fig. 2, but for the WS₂/hBN/Co system.

FIG. 9. Same as Fig. 2, but for the WS₂/hBN/Ni system.

calculations provide useful insight to interpret experimental properties of TMDC/hBN/(Co, Ni) devices, for instance related to spin injection, spin tunneling, and optics. Finally, our extracted parameters can be used as input for transport simulations and additional studies of excitonic effects.

ACKNOWLEDGMENTS

We thank A. Chernikov for helpful discussions. This work was supported by the Deutsche Forschungsgemeinschaft (DFG, German Research Foundation) Project-ID 314695032

SFB 1277, DFG SPP 1666, the European Unions Horizon 2020 research and innovation program under Grant No. 785219, the Alexander von Humboldt Foundation and Capes (Grant No. 99999.000420/2016-06).

APPENDIX: FURTHER DFT RESULTS

For completeness, in Figs. 7, 8, and 9 we show the calculated band structure, density of states, and low energy model fits for the MoS₂/hBN/Ni, WS₂/hBN/Co, and WS₂/hBN/Ni heterostructures.

- [1] I. Žutić, J. Fabian, and S. Das Sarma, *Rev. Mod. Phys.* **76**, 323 (2004).
- [2] W. Han, R. K. Kawakami, M. Gmitra, and J. Fabian, *Nat. Nanotechnol.* **9**, 794 (2014).
- [3] J. Fabian, A. Matos-Abiague, C. Ertler, P. Stano, and I. Žutić, *Acta Phys. Slov.* **57**, 565 (2007).
- [4] W. Liu, P. K. J. Wong, and Y. Xu, *Prog. Mater. Sci.* **99**, 27 (2019).
- [5] N. Briggs, S. Subramanian, Z. Lin, X. Li, X. Zhang, K. Zhang, K. Xiao, D. Geohegan, R. Wallace, L.-Q. Chen, M. Terrones, A. Ebrahimi, S. Das, J. Redwing, C. Hinkle, K. Momeni, A. van Duin, V. Crespi, S. Kar, and J. A. Robinson, *2D Mater.* **6**, 022001 (2019).
- [6] J. H. Zhiqian Yuan and K. Liu, *Crystals* **7**, 265 (2017).
- [7] Z. Hu, Z. Wu, C. Han, J. He, Z. Ni, and W. Chen, *Chem. Soc. Rev.* **47**, 3100 (2018).
- [8] M. V. Kamalakar, A. Dankert, J. Bergsten, T. Ive, and S. P. Dash, *Sci. Rep.* **4**, 6146 (2014).
- [9] W. Fu, P. Makk, R. Maurand, M. Bräuninger, and C. Schönenberger, *J. Appl. Phys.* **116**, 074306 (2014).
- [10] M. Drögeler, C. Franzen, F. Volmer, T. Pohlmann, L. Banszerus, M. Wolter, K. Watanabe, T. Taniguchi, C. Stampfer, and B. Beschoten, *Nano Lett.* **16**, 3533 (2016).
- [11] M. Drögeler, F. Volmer, M. Wolter, B. Terrés, K. Watanabe, T. Taniguchi, G. Güntherodt, C. Stampfer, and B. Beschoten, *Nano Lett.* **14**, 6050 (2014).
- [12] M. V. Kamalakar, A. Dankert, P. J. Kelly, and S. P. Dash, *Sci. Rep.* **6**, 21168 (2016).
- [13] M. V. Kamalakar, C. Groenveld, A. Dankert, and S. P. Dash, *Nat. Commun.* **6**, 6766 (2015).
- [14] M. Gurram, S. Omar, and B. J. van Wees, *2D Mater.* **5**, 032004 (2018).
- [15] M. Gurram, S. Omar, and B. J. van Wees, *Nat. Commun.* **8**, 248 (2017).
- [16] L. Banszerus, M. Schmitz, S. Engels, J. Dauber, M. Oellers, F. Haupt, K. Watanabe, T. Taniguchi, B. Beschoten, and C. Stampfer, *Sci. Adv.* **1**, e1500222 (2015).
- [17] N. Petrone, C. R. Dean, I. Meric, A. M. Van Der Zande, P. Y. Huang, L. Wang, D. Muller, K. L. Shepard, and J. Hone, *Nano Lett.* **12**, 2751 (2012).

- [18] V. E. Calado, S.-E. Zhu, S. Goswami, Q. Xu, K. Watanabe, T. Taniguchi, G. C. A. M. Janssen, and L. M. K. Vandersypen, *Appl. Phys. Lett.* **104**, 023103 (2014).
- [19] K. Zollner, M. Gmitra, T. Frank, and J. Fabian, *Phys. Rev. B* **94**, 155441 (2016).
- [20] M. Gmitra, D. Kochan, P. Högl, and J. Fabian, *Phys. Rev. B* **93**, 155104 (2016).
- [21] M. Gmitra and J. Fabian, *Phys. Rev. B* **92**, 155403 (2015).
- [22] A. W. Cummings, J. H. Garcia, J. Fabian, and S. Roche, *Phys. Rev. Lett.* **119**, 206601 (2017).
- [23] S. Zihlmann, A. W. Cummings, J. H. Garcia, M. Kedves, K. Watanabe, T. Taniguchi, C. Schönenberger, and P. Makk, *Phys. Rev. B* **97**, 075434 (2018).
- [24] S. Omar and B. J. van Wees, *Phys. Rev. B* **97**, 045414 (2018).
- [25] A. Avsar, D. Unuchek, J. Liu, O. L. Sanchez, K. Watanabe, T. Taniguchi, B. Özyilmaz, and A. Kis, *ACS Nano* **11**, 11678 (2017).
- [26] J. C. Leutenantsmeyer, J. Ingla-Aynés, J. Fabian, and B. J. van Wees, *Phys. Rev. Lett.* **121**, 127702 (2018).
- [27] J. Xu, T. Zhu, Y. K. Luo, Y.-M. Lu, and R. K. Kawakami, *Phys. Rev. Lett.* **121**, 127703 (2018).
- [28] Y. K. Luo, J. Xu, T. Zhu, G. Wu, E. J. McCormick, W. Zhan, M. R. Neupane, and R. K. Kawakami, *Nano Lett.* **17**, 3877 (2017).
- [29] L. Li, Y. Yu, G. J. Ye, Q. Ge, X. Ou, H. Wu, D. Feng, X. H. Chen, and Y. Zhang, *Nat. Nanotechnol.* **9**, 372 (2014).
- [30] I. Zutic, J. Fabian, and S. C. Erwin, *IBM J. Res. Dev.* **50**, 121 (2006).
- [31] S. Liang, H. Yang, A. Djeflal, B. Tao, S. Mc-Murtry, S. Mangin, and Y. Lu, *J. Appl. Phys.* **122**, 164301 (2017).
- [32] S. Ahmed and J. Yi, *Nano-Micro Lett.* **9**, 50 (2017).
- [33] M. Kurpas, M. Gmitra, and J. Fabian, *Phys. Rev. B* **94**, 155423 (2016).
- [34] M. Kurpas, M. Gmitra, and J. Fabian, *J. Phys. D: Appl. Phys.* **51**, 174001 (2018).
- [35] A. Avsar, J. Y. Tan, X. Luo, K. H. Khoo, Y. Yeo, K. Watanabe, T. Taniguchi, S. Y. Quek, and B. Özyilmaz, *Nano Lett.* **17**, 5361 (2017).
- [36] J. Qiao, X. Kong, Z.-X. Hu, F. Yang, and W. Ji, *Nat. Commun.* **5**, 4475 (2014).
- [37] H. Liu, A. T. Neal, Z. Zhu, Z. Luo, X. Xu, D. Tománek, and P. D. Ye, *ACS Nano* **8**, 4033 (2014).
- [38] A. Kormányos, G. Burkard, M. Gmitra, J. Fabian, V. Zólyomi, N. D. Drummond, and V. Fal'ko, *2D Mater.* **2**, 022001 (2015).
- [39] G.-B. Liu, D. Xiao, Y. Yao, X. Xu, and W. Yao, *Chem. Soc. Rev.* **44**, 2643 (2015).
- [40] P. Tonndorf, R. Schmidt, P. Böttger, X. Zhang, J. Börner, A. Liebig, M. Albrecht, C. Kloc, O. Gordan, D. R. T. Zahn, S. Michaelis de Vasconcellos, and R. Bratschitsch, *Opt. Express* **21**, 4908 (2013).
- [41] S. Tongay, J. Zhou, C. Ataca, K. Lo, T. S. Matthews, J. Li, J. C. Grossman, and J. Wu, *Nano Lett.* **12**, 5576 (2012).
- [42] G. Eda, H. Yamaguchi, D. Voiry, T. Fujita, M. Chen, and M. Chhowalla, *Nano Lett.* **11**, 5111 (2011).
- [43] D. Xiao, G.-B. Liu, W. Feng, X. Xu, and W. Yao, *Phys. Rev. Lett.* **108**, 196802 (2012).
- [44] S. A. Vitale, D. Nezych, J. O. Varghese, P. Kim, N. Gedik, P. Jarillo-Herrero, D. Xiao, and M. Rothschild, *Small* **14**, 1801483 (2018).
- [45] F. Langer, C. P. Schmid, S. Schlauderer, M. Gmitra, J. Fabian, P. Nagler, C. Schüller, T. Korn, P. G. Hawkins, J. T. Steiner, U. Huttner, S. W. Koch, M. Kira, and R. Huber, *Nature (London)* **557**, 76 (2018).
- [46] J. R. Schaibley, H. Yu, G. Clark, P. Rivera, J. S. Ross, K. L. Seyler, W. Yao, and X. Xu, *Nat. Rev. Mater.* **1**, 16055 (2016).
- [47] Y. Ye, J. Xiao, H. Wang, Z. Ye, H. Zhu, M. Zhao, Y. Wang, J. Zhao, X. Yin, and X. Zhang, *Nat. Nanotechnol.* **11**, 598 (2016).
- [48] D. Zhong, K. L. Seyler, X. Linpeng, R. Cheng, N. Sivadas, B. Huang, E. Schmidgall, T. Taniguchi, K. Watanabe, M. A. McGuire, W. Yao, D. Xiao, K.-M. C. Fu, and X. Xu, *Sci. Adv.* **3**, e1603113 (2017).
- [49] A. Srivastava, M. Sidler, A. V. Allain, D. S. Lembke, A. Kis, and A. Imamolu, *Nat. Phys.* **11**, 141 (2015).
- [50] G. Aivazian, Z. Gong, A. M. Jones, R. L. Chu, J. Yan, D. G. Mandrus, C. Zhang, D. Cobden, W. Yao, and X. Xu, *Nat. Phys.* **11**, 148 (2015).
- [51] Y. Li, J. Ludwig, T. Low, A. Chernikov, X. Cui, G. Arefe, Y. D. Kim, A. M. van der Zande, A. Rigosi, H. M. Hill, S. H. Kim, J. Hone, Z. Li, D. Smirnov, and T. F. Heinz, *Phys. Rev. Lett.* **113**, 266804 (2014).
- [52] D. MacNeill, C. Heikes, K. F. Mak, Z. Anderson, A. Kormányos, V. Zólyomi, J. Park, and D. C. Ralph, *Phys. Rev. Lett.* **114**, 037401 (2015).
- [53] Y. Ji, Y. Song, J. Zou, and W. Mi, *Phys. Chem. Chem. Phys.* **20**, 6100 (2018).
- [54] N. Li, J. Zhang, Y. Xue, T. Zhou, and Z. Yang, *Phys. Chem. Chem. Phys.* **20**, 3805 (2018).
- [55] J. Qi, X. Li, Q. Niu, and J. Feng, *Phys. Rev. B* **92**, 121403(R) (2015).
- [56] Q. Zhang, S. A. Yang, W. Mi, Y. Cheng, and U. Schwingenschlögl, *Adv. Mater.* **28**, 959 (2016).
- [57] L. Xu, M. Yang, L. Shen, J. Zhou, T. Zhu, and Y. P. Feng, *Phys. Rev. B* **97**, 041405(R) (2018).
- [58] C. Zhao, T. Norden, P. Zhang, P. Zhao, Y. Cheng, F. Sun, J. P. Parry, P. Taheri, J. Wang, Y. Yang, T. Scrace, K. Kang, S. Yang, G. X. Miao, R. Sabirianov, G. Kioseoglou, W. Huang, A. Petrou, and H. Zeng, *Nat. Nanotechnol.* **12**, 757 (2017).
- [59] K. L. Seyler, D. Zhong, B. Huang, X. Linpeng, N. P. Wilson, T. Taniguchi, K. Watanabe, W. Yao, D. Xiao, M. A. McGuire, K. M. C. Fu, and X. Xu, *Nano Lett.* **18**, 3823 (2018).
- [60] B. Peng, Q. Li, X. Liang, P. Song, J. Li, K. He, D. Fu, Y. Li, C. Shen, H. Wang, C. Wang, T. Liu, L. Zhang, H. Lu, X. Wang, J. Zhao, J. Xie, M. Wu, L. Bi, L. Deng, and K. P. Loh, *ACS Nano* **11**, 12257 (2017).
- [61] Z. Zhang, X. Ni, H. Huang, L. Hu, and F. Liu, *Phys. Rev. B* **99**, 115441 (2019).
- [62] K. Zollner, P. E. Faria Junior, and J. Fabian, *Phys. Rev. B* **100**, 085128 (2019).
- [63] D. Somvanshi, S. Kallatt, C. Venkatesh, S. Nair, G. Gupta, J. K. Anthony, D. Karmakar, and K. Majumdar, *Phys. Rev. B* **96**, 205423 (2017).
- [64] O. L. Sanchez, D. Ovchinnikov, S. Misra, A. Allain, and A. Kis, *Nano Lett.* **16**, 5792 (2016).
- [65] M. Farmanbar and G. Brocks, *Phys. Rev. B* **93**, 085304 (2016).
- [66] M. Farmanbar and G. Brocks, *Phys. Rev. B* **91**, 161304(R) (2015).
- [67] X. Cui, E.-M. Shih, L. A. Jauregui, S. H. Chae, Y. D. Kim, B. Li, D. Seo, K. Pistunova, J. Yin, J.-H. Park, H.-J. Choi, Y. H.

- Lee, K. Watanabe, T. Taniguchi, P. Kim, C. R. Dean, and J. C. Hone, *Nano Lett.* **17**, 4781 (2017).
- [68] Y. Zhao, K. Xu, F. Pan, C. Zhou, F. Zhou, and Y. Chai, *Adv. Funct. Mater.* **27**, 1603484 (2017).
- [69] T. Garandel, R. Arras, X. Marie, P. Renucci, and L. Calmels, *Phys. Rev. B* **95**, 075402 (2017).
- [70] A. Rai, H. Movva, A. Roy, D. Taneja, S. Chowdhury, and S. Banerjee, *Crystals* **8**, 316 (2018).
- [71] D. S. Schulman, A. J. Arnold, and S. Das, *Chem. Soc. Rev.* **47**, 3037 (2018).
- [72] Y. Guo, Y. Han, J. Li, A. Xiang, X. Wei, S. Gao, and Q. Chen, *ACS Nano* **8**, 7771 (2014).
- [73] M. Zhu, W. Luo, N. Wu, X.-A. Zhang, and S. Qin, *Appl. Phys. Lett.* **112**, 183102 (2018).
- [74] J. Su, L.-P. Feng, X. Zheng, C. Hu, H. Lu, and Z. Liu, *ACS Appl. Mater. Interfaces* **9**, 40940 (2017).
- [75] J. Wang, Q. Yao, C.-W. Huang, X. Zou, L. Liao, S. Chen, Z. Fan, K. Zhang, W. Wu, X. Xiao, C. Jiang, and W.-W. Wu, *Adv. Mater.* **28**, 8302 (2016).
- [76] N. Kaushik, D. Karmakar, A. Nipane, S. Karande, and S. Lodha, *ACS Appl. Mater. Interfaces* **8**, 256 (2016).
- [77] S. Liang, H. Yang, P. Renucci, B. Tao, P. Laczkowski, S. McMurtry, G. Wang, X. Marie, J.-M. George, S. Petit-Watelot, A. Djéffal, S. Mangin, H. Jaffrès, and Y. Lu, *Nat. Commun.* **8**, 14947 (2017).
- [78] W. Wang, Y. Liu, L. Tang, Y. Jin, T. Zhao, and F. Xiu, *Sci. Rep.* **4**, 6928 (2014).
- [79] A. Dankert, L. Langouche, M. V. Kamalakar, and S. P. Dash, *ACS Nano* **8**, 476 (2014).
- [80] N. Hayakawa, I. Muneta, T. Ohashi, K. Matsuura, J. Shimizu, K. Kakushima, K. Tsutsui, and H. Wakabayashi, *Jpn. J. Appl. Phys.* **57**, 04FP13 (2018).
- [81] H. M. W. Khalil, M. F. Khan, J. Eom, and H. Noh, *ACS Appl. Mater. Interfaces* **7**, 23589 (2015).
- [82] Y. Liu, H. Wu, H.-C. Cheng, S. Yang, E. Zhu, Q. He, M. Ding, D. Li, J. Guo, N. O. Weiss, Y. Huang, and X. Duan, *Nano Lett.* **15**, 3030 (2015).
- [83] Y. Song and H. Dery, *Phys. Rev. Lett.* **111**, 026601 (2013).
- [84] K. Tian, Z. Yue, D. Maggini, M. E. Raikh, and A. Tiwari, *Phys. Rev. B* **95**, 174428 (2017).
- [85] J. R. Durán Retamal, D. Periyangounder, J.-J. Ke, M.-L. Tsai, and J.-H. He, *Chem. Sci.* **9**, 7727 (2018).
- [86] H. Schmidt, F. Giustiniano, and G. Eda, *Chem. Soc. Rev.* **44**, 7715 (2015).
- [87] S. L. Li, K. Wakabayashi, Y. Xu, S. Nakaharai, K. Komatsu, W. W. Li, Y. F. Lin, A. Aparecido-Ferreira, and K. Tsukagoshi, *Nano Lett.* **13**, 3546 (2013).
- [88] H. Ochoa and R. Roldán, *Phys. Rev. B* **87**, 245421 (2013).
- [89] T. Habe and M. Koshino, *Phys. Rev. B* **93**, 075415 (2016).
- [90] F. Yang, L. Wang, and M. W. Wu, *Phys. Rev. B* **92**, 155414 (2015).
- [91] F. Yang and M. W. Wu, *Phys. Rev. B* **93**, 235433 (2016).
- [92] P. Hohenberg and W. Kohn, *Phys. Rev.* **136**, B864 (1964).
- [93] P. Giannozzi, S. Baroni, N. Bonini, M. Calandra, R. Car, C. Cavazzoni, D. Ceresoli, G. L. Chiarotti, M. Cococcioni, I. Dabo, A. D. Corso, S. Fabris, G. Fratesi, S. de Gironcoli, R. Gebauer, U. Gerstmann, C. Gougoussis, A. Kokalj, M. Lazzeri, L. Martin-Samos *et al.*, *J. Phys.: Condens. Matter* **21**, 395502 (2009).
- [94] G. Kresse and D. Joubert, *Phys. Rev. B* **59**, 1758 (1999).
- [95] J. P. Perdew, K. Burke, and M. Ernzerhof, *Phys. Rev. Lett.* **77**, 3865 (1996).
- [96] A. I. Liechtenstein, V. I. Anisimov, and J. Zaanen, *Phys. Rev. B* **52**, R5467 (1995).
- [97] J.-C. Tung, H.-R. Fuh, and G.-Y. Guo, *Phys. Rev. B* **86**, 024435 (2012).
- [98] Y. S. Mohammed, Y. Yan, H. Wang, K. Li, and X. Du, *J. Magn. Magn. Mater.* **322**, 653 (2010).
- [99] S. Grimme, *J. Comput. Chem.* **27**, 1787 (2006).
- [100] V. Barone, M. Casarin, D. Forrer, M. Pavone, M. Sambri, and A. Vittadini, *J. Comput. Chem.* **30**, 934 (2009).
- [101] L. Bengtsson, *Phys. Rev. B* **59**, 12301 (1999).
- [102] M. Rohlfing and S. G. Louie, *Phys. Rev. B* **62**, 4927 (2000).
- [103] D. Y. Qiu, F. H. da Jornada, and S. G. Louie, *Phys. Rev. Lett.* **111**, 216805 (2013).
- [104] R. Soklaski, Y. Liang, and L. Yang, *Appl. Phys. Lett.* **104**, 193110 (2014).
- [105] B. Scharf, G. Xu, A. Matos-Abiague, and I. Žutić, *Phys. Rev. Lett.* **119**, 127403 (2017).
- [106] B. Scharf, D. Van Tuan, I. Žutić, and H. Dery, *J. Phys.: Condens. Matter* **31**, 203001 (2019).
- [107] P. E. Faria Junior, M. Kurpas, M. Gmitra, and J. Fabian, *Phys. Rev. B* **100**, 115203 (2019).
- [108] H. Haug and S. W. Koch, *Quantum Theory of the Optical and Electronic Properties of Semiconductors: Fifth Edition* (World Scientific, Singapore, 2009).
- [109] N. S. Rytova, *Moscow Univ. Phys. Bull.* **3**, 18 (1967).
- [110] L. V. Keldysh, *Sov. J. Exper. Theor. Phys. Lett.* **29**, 658 (1979).
- [111] P. Cudazzo, I. V. Tokatly, and A. Rubio, *Phys. Rev. B* **84**, 085406 (2011).
- [112] T. C. Berkelbach, M. S. Hybertsen, and D. R. Reichman, *Phys. Rev. B* **88**, 045318 (2013).
- [113] A. Chernikov, T. C. Berkelbach, H. M. Hill, A. Rigosi, Y. Li, O. B. Aslan, D. R. Reichman, M. S. Hybertsen, and T. F. Heinz, *Phys. Rev. Lett.* **113**, 076802 (2014).
- [114] F. Wu, F. Qu, and A. H. MacDonald, *Phys. Rev. B* **91**, 075310 (2015).
- [115] H. Haug and S. W. Koch, *Quantum Theory of the Optical and Electronic Properties of Semiconductors: Fifth Edition* (World Scientific, Singapore, 2009).
- [116] S. R. Bahn and K. W. Jacobsen, *Comput. Sci. Eng.* **4**, 56 (2002).
- [117] C. M. Singal and T. P. Das, *Phys. Rev. B* **16**, 5068 (1977).
- [118] C. Kittel, *Introduction to Solid State Physics* (Wiley, New York, 2004).
- [119] A. Catellani, M. Posternak, A. Baldereschi, and A. J. Freeman, *Phys. Rev. B* **36**, 6105 (1987).
- [120] N. Wakabayashi, H. G. Smith, and R. M. Nicklow, *Phys. Rev. B* **12**, 659 (1975).
- [121] W. J. Schutte, J. L. De Boer, and F. Jellinek, *J. Solid State Chem.* **70**, 207 (1987).
- [122] M. Bokdam, G. Brocks, M. I. Katsnelson, and P. J. Kelly, *Phys. Rev. B* **90**, 085415 (2014).
- [123] P. Lazić, G. M. Sipahi, R. K. Kawakami, and I. Žutić, *Phys. Rev. B* **90**, 085429 (2014).
- [124] K. Zollner, P. E. Faria Junior, and J. Fabian, *Phys. Rev. B* **100**, 195126 (2019).

- [125] A. V. Stier, N. P. Wilson, K. A. Velizhanin, J. Kono, X. Xu, and S. A. Crooker, *Phys. Rev. Lett.* **120**, 057405 (2018).
- [126] Z. Jiang, Z. Liu, Y. Li, and W. Duan, *Phys. Rev. Lett.* **118**, 266401 (2017).
- [127] A. Raja, A. Chaves, J. Yu, G. Arefe, H. M. Hill, A. F. Rigosi, T. C. Berkelbach, P. Nagler, C. Schüller, T. Korn *et al.*, *Nat. Commun.* **8**, 15251 (2017).
- [128] S.-Y. Chen, Z. Lu, T. Goldstein, J. Tong, A. Chaves, J. Kunstmann, L. Cavalcante, T. Wozniak, G. Seifert, D. Reichman *et al.*, *Nano Lett.* **19**, 2464 (2019).
- [129] G. Catarina, N. M. R. Peres, and J. Fernández-Rossier, *2D Mater.* **7**, 025011 (2020).
- [130] J. C. G. Henriques, G. Catarina, A. T. Costa, J. Fernández-Rossier, and N. M. R. Peres, *Phys. Rev. B* **101**, 045408 (2020).